Tungsten control in type-I ELMy H-mode plasmas on EAST

Zong Xu[1,2] · Zhen-Wei Wu[3] · Ling Zhang[3] · Yun-Xing Cheng[3,4] ·
Wei Gao[3] · Xiao-Dong Lin[1,2] · Xiang Gao[1,2,3] · Ying-Jie Chen[3] · Yue-Heng Huang[1,2] ·
Juan Huang[3] · Qing Zang[1,2,3] · Yin-Xian Jie[1,2,3] · Yan-Min Duan[3] ·
Ying-Ying Li[3] · Hai-Qing Liu[3] · Guo-Sheng Xu[3] · EAST team[3]

Abstract The first experimental investigation of the tungsten behavior in ELMy H-mode plasmas with co-/counter neutral beam injection (NBI) and unfavorable/favorable B_t was performed on EAST. Tungsten was found to accumulate easily in ELMy H-mode plasma with co-NBI heating and unfavorable B_t. Thus, in this case the tungsten concentration can exceed 10^{-4}, resulting in degradation of the plasma confinement and periodic H–L transitions. To reduce the tungsten concentration in steady-state type-I ELMy H-mode operation, counter-NBI is applied to modify the density and temperature and brake the plasma toroidal rotation. The applied counter-NBI decreases the PHZ $+ E_r$ inward pinch velocity and reverses the direction of neoclassical inward convection, thus decreasing the tungsten concentration from $\sim 7 \times 10^{-5}$ to $\sim 2 \times 10^{-5}$ in type-I ELMy H-mode plasma with favorable B_t. A comparison of the effects of different B_t directions on the tungsten behavior also shows that favorable B_t is beneficial for reducing the tungsten concentration in the core plasma. These results imply that counter-NBI with favorable B_t can effectively prevent tungsten accumulation and expand the operating window for exploring steady-state type-I ELMy H-mode operation of EAST.

Keywords Tungsten accumulation · Counter-NBI · Favorable B_t · ELMy H-mode · EAST

✉ Zhen-Wei Wu
zwwu@ipp.ac.cn

✉ Ling Zhang
zhangling@ipp.ac.cn

1 Advanced Energy Research Center, Shenzhen University, Shenzhen 518060, China

2 Key Laboratory of Optoelectronic Devices and Systems of Ministry of Education and Guangdong Province, College of Optoelectronic Engineering, Shenzhen University, Shenzhen 518060, China

3 Institute of Plasma Physics, Chinese Academy of Science, Hefei 230031, China

4 University of Science & Technology of China, Hefei 230031, China

1 Introduction

Tungsten is a good candidate for plasma-facing materials in future fusion devices such as ITER and CFETR. Its intrinsic benefits include a high melting point, a low sputtering yield, and a low tritium retention. However, tungsten accumulation in the core plasma can result in serious radiation losses, the degradation of the overall energy confinement [1], magnetohydrodynamic (MHD) instabilities [2], or even disruptions [3–5]. For ITER, the tungsten concentration ($C_W = n_W/n_e$, where n_W and n_e are the tungsten and electron densities, respectively) must be less than 10^{-4} to avoid unacceptable radiative cooling [6]. It is therefore important to avoid tungsten accumulation in the high-confinement regime in devices with tungsten

divertor plates, where tungsten atoms can be sputtered from the divertor plates by giant edge-localized modes (ELMs) [7, 8]. Methods of reducing the stored energy radiated by tungsten in the central plasma are a concern for the economical operation of future commercial reactors [9].

Previous investigations have shown that core impurity accumulation is driven mainly by neoclassical inward convection [10], and the negative radial electric field (E_r) is responsible for inward impurity transport [11, 12]. In addition, the inward pinch of high-Z impurities (PHZ) attributed to the atomic processes of ionization and recombination also plays a role in core tungsten accumulation in a toroidally rotating plasma [12–14]. Thus, to suppress and avoid tungsten accumulation, these inward pinch velocities must be reduced and well controlled. Theoretical predictions and experimental observations have shown that neoclassical convection can be controlled by changing the density and temperature gradients [15–17], and the PHZ and E_r pinch depend strongly on the toroidal rotation velocity of the background plasma [12]. Turbulent transport due to, for example, the ion temperature gradient (ITG) mode and trapped electron mode (TEM), can also affect tungsten transport [18–20], but it is much weaker than neoclassical transport in the central region of a toroidally rotating plasma, as has been found in JET and the ASDEX Upgrade [21–23]. Turbulent transport can be enhanced by decreasing the ion-to-electron temperature ratio (T_i/T_e) [24, 25] so as to increase the impurity diffusivity and suppress impurity accumulation. Neutral beam injection (NBI), which can alter the density and temperature and change the toroidal rotation velocity, will be used to study the tungsten behavior in the core of an EAST type-I ELMy H-mode plasma, because the ELMy H-mode with a low ELM frequency (f_{ELM}) of dozens of hertz has inevitably been found to result in strong impurity accumulation in EAST [26–28]. Here, the effects of neoclassical transport [10] and the PHZ and E_r pinch on the tungsten behavior in the type-I ELMy H-mode regime are studied. In addition, the effect of turbulent transport on tungsten transport is briefly discussed.

The remainder of the paper is structured as follows. Section 2 describes the NBI systems and relevant diagnostics in EAST, and Sect. 3 reports the experimental investigation of the tungsten behavior in ELMy H-mode plasmas with co-/counter-NBI and different toroidal field (TF) directions. In Sect. 4, a summary and discussion are presented.

2 Experimental setup

This work is based on the EAST tokamak device. EAST is a full superconducting device that was designed to operate with major radii R of 1.7–1.9 m, minor radii a of 0.4–0.45 m, a maximum TF strength B_t of 3.5 T, a maximum plasma current I_p of 1 MA, an elongation k of 1.2–2, and a triangularity δ of < 0.8. Since the 2014 campaign, EAST has been upgraded to facilitate progress in achieving long-pulse stable high-performance plasma operation [pulse length > 1000 s, central electron temperature $T_{e0} > 10$ keV, normalized beta $\beta_N > 2$, and $n_e \sim n_{GW}$, where $n_{GW} = I_p/\pi a^2$ (10^{20} m^{-3})]. For these purposes, several auxiliary heating systems have been developed to provide effective heating and current drive for EAST [29, 30]. As the auxiliary heating power is increased, the materials of plasma-facing components (PFCs) are replaced at different positions of the inner wall to improve the heat exhaust ability [31]. The main PFC materials in EAST are molybdenum tiles mounted on the first wall of the vacuum chamber, SiC-coated graphite tiles fixed in the lower divertor, and W/Cu mono-blocks installed in the upper divertor [32].

Two sets of NBI systems have been installed on EAST since the 2014 and 2015 campaigns [33, 34]. The NBI system in EAST consists of two sets of neutral beam injectors. The maximum beam power of each injector is 4 MW, and the maximum beam energy ranges from 50 to 80 keV. One injector has two ion sources which with an independent beam channel and can be operated independently. The layout of the EAST NBI system is shown in Fig. 1. For anticlockwise I_p, the tangential direction of each injector (the co-I_p direction is denoted as co-NBI, whereas the counter-I_p direction is denoted as counter-NBI) and the unfavorable direction of B_t (counter-I_p direction) are shown in the figure.

To investigate the tungsten behavior in core plasmas with different NBI and B_t directions, three newly
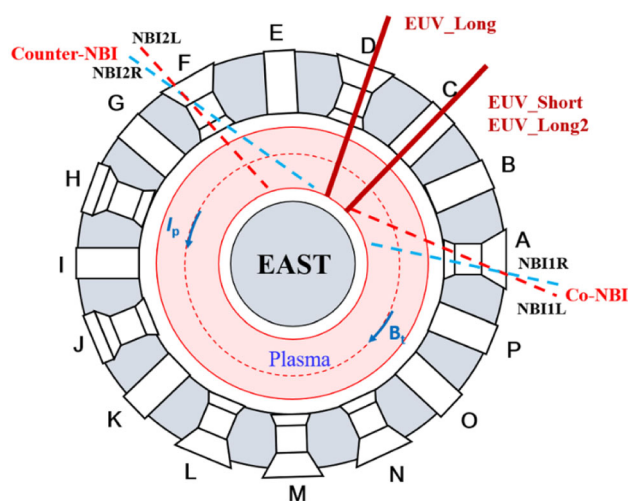
Fig. 1 (Color online) Directions of plasma current I_p and toroidal field B_t, and layout of two sets of NBI systems and EUV spectrometers on EAST

developed extreme ultraviolet (EUV) spectrometers (EUV_Short, EUV_Long, and EUV_Long2 in Fig. 1) will be used. EUV_Short and EUV_Long [35, 36] operate in wavelength ranges of 20–50 Å and 20–500 Å, respectively, and both have good spectral resolution for measuring the chord-integrated intensity of line emission from tungsten. Other relevant diagnostics include a Thomson scattering system for observing the profiles of the electron temperature and density, a polarimeter–interferometer for monitoring the profiles of the electron density and safety factor, a fast CCD camera for detecting the plasma position [37], and charge exchange recombination spectroscopy for monitoring the ion temperature profile and toroidal rotation velocity of the background plasma.

3 Experimental results

### 3.1 Tungsten accumulation at high toroidal rotation velocity

Since 2014, EAST has been used to access advanced regimes with steady-state high-performance plasma in ITER-like tungsten divertor operation [38–41]. However, the accumulation of tungsten that is transported from the divertor by regular collisions or large ELMy impacts [42, 43] always degrades the performance of H-mode plasma. In this section, the behavior of tungsten under a combination of NBI and lower hybrid wave (LHW) heating in the type-I ELMy H-mode regime is investigated to explore suitable heating scenarios without high-Z impurity accumulation and to develop the steady-state long-pulse and high-performance regime.

Type-I ELMy H-mode discharges with the ITER-like tungsten divertor are selected to investigate the tungsten behavior in the core plasma. In the discharge of shot #63723, type-I ELMs with $f_{ELM} \sim 80$ Hz were obtained when additional co-NBI was performed during the LHW heating phase, as shown in Fig. 2. This discharge was performed in the upper single-null (USN) configuration with an unfavorable B_t direction (counter-I_p direction, where the direction of $B_t \times \nabla B_t$ points away from the divertor X-point) at $B_t = 2.3$T, $I_p = 0.5$ MA, a line-averaged electron density $\overline{n}_e$ of $\sim 2.5 \times 10^{19}$ m^{-3}, and a safety factor at 95% of the magnetic flux, q_{95}, of 5, where the source power of LHW and co-NBI heating is 1.5 and 4.0 MW, respectively. In this shot, the toroidal rotation velocity of the background plasma can be driven to a quite high level [a central toroidal rotation velocity $V_t(0)$ of $\sim$ 140 km/s] because co-NBI heating is applied.

The emission from high ionization stages of Li, C, Fe, Cu, Mo, and W is detected by EUV spectrometers at wavelengths of 20–150 Å [35, 36]. Figure 3a–c shows the
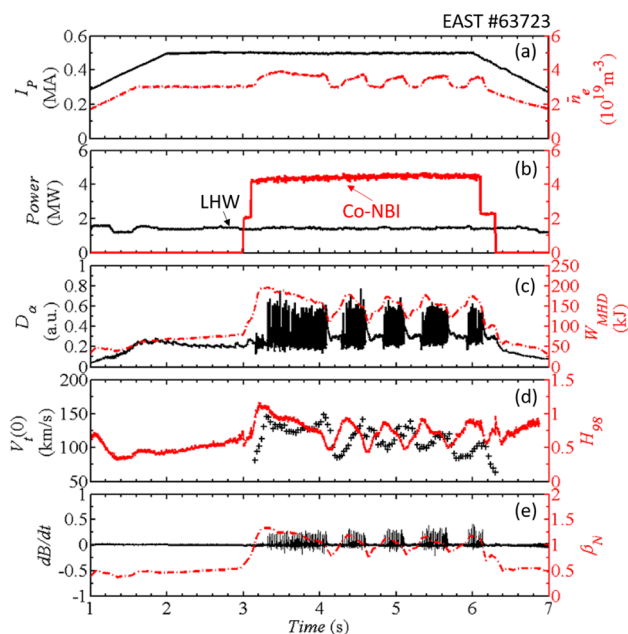
Fig. 2 (Color online) Waveforms of a typical tungsten accumulation shot, #63723. **a** Plasma current I_p and line-averaged electron density $\overline{n}_e$, **b** total LHW and NBI heating power, **c** intensity of divertor D_α emission, and plasma stored energy W_{MHD}, **d** central toroidal rotation velocity $V_t(0)$ and energy confinement factor H_{98}, and **e** external Mirnov coil signal and normalized beta β_N
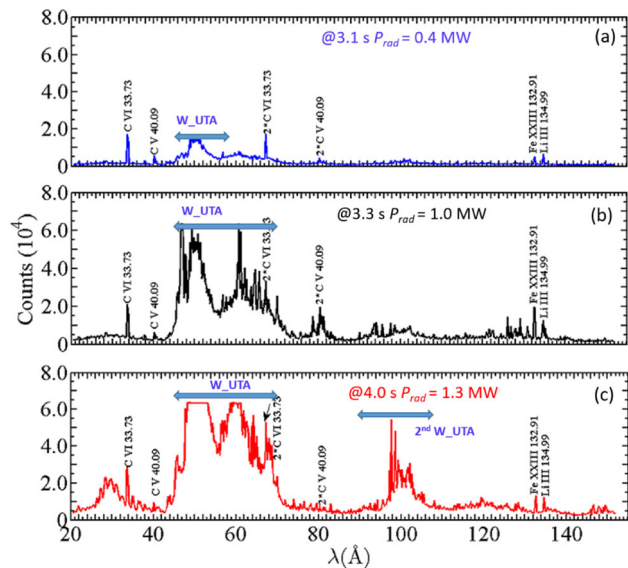
Fig. 3 (Color online) EUV spectra from shot #63723 in wavelength range of 20–150 Å at times of (a) 3.1 s, (b) 3.3 s, and (c) 4.1 s

EUV spectra and total radiative power (P_{rad}) at 3.1, 3.3, and 4.1 s, respectively. The stronger emission lines, such as Li III (134.99 Å), C VI (33.73 Å), and Fe XXIII (132.91 Å), and the first- and second-order tungsten emission in the unresolved transition array (W-UTA) are labeled. C_W in core plasma is evaluated as the W-UTA

intensity at 45–70 Å, which is composed of W^{24+}–W^{45+}. The C_W calculation method is analyzed and introduced in literature [44]. The W-UTA intensity is found to increase sharply with increase in P_{rad}. In particular, in Fig. 3b and c, when P_{rad} is changed from 1.0 to 1.3 MW, the intensity of the first-order W-UTA becomes saturated, and the second-order W-UTA emission appears and becomes more intense, whereas the intensity of emission from other impurities remains relatively low. This result confirmed that tungsten accumulates easily in the core plasma when co-NBI is performed and makes a large contribution to this important radiation.

The process of tungsten accumulation is shown in Fig. 4a and b. C_W increases continually during each tungsten accumulation phase, and the radiation profile becomes progressively peaked correspondingly. Noticeably, in the first phase of the H-mode, because $q(0)$ is slightly less than 1 [Fig. 5d], core MHD activity ($m/n = 1/1$) begins and is observed on the spectrogram of the core soft X-ray emission signals from 3.0 to 3.6 s, as shown in Fig. 4c. This core MHD activity may enhance the impurity diffusivity and decrease the neoclassical convection [45, 46], which suppresses further increases in C_W in the core plasma. Although this MHD activity vanishes after 3.6 s, C_W continues to grow. In this case, tungsten accumulation results in a larger radiated power loss; thus, a transition back to the L-mode phase occurs after approximately one energy confinement time τ_E [$\tau_E = W_{MHD}/(P_{total} - dW_{MHD}/dt)$]. These sequences of tungsten accumulation

Fig. 4 (Color online) Analysis of tungsten accumulation from 3.0 to 4.8 s in shot #63723. a Tungsten concentration C_W, b radiation profile measured by 64-channel fast bolometer system and W-UTA emission intensity, and c spectrogram of central chord of soft X-ray emission signals

and H–L transitions can repeat several times with a period of approximately 3–$6\tau_E$. In each tungsten accumulation phase, the effective charge number Z_{eff} increases from ~ 3 to ~ 3.5, and C_W increases from $\sim 0.23 \times 10^{-4}$ to $\sim 1.6 \times 10^{-4}$; thus, the power radiation fraction P_{rad}/P_{total} increases from $\sim 15\%$ to a peak value of $\sim 50\%$. The energy confinement factors H_{98} and β_N are clearly attenuated during each tungsten accumulation process, as shown in Fig. 2.

Figure 5a–d shows the electron density, electron temperature, ion temperature, and safety factor profiles, respectively, during the L-mode phase (at ~ 3.1 s, blue line) and before (at ~ 3.3 s, red line) and during (at ~ 4.0 s, black line) tungsten accumulation in the H-mode phase of shot #63723. The strong radiative power loss caused by tungsten accumulation changes the profiles and results in an aggravated plasma performance and steady-state operation, as follows. (i) The electron temperature profile inside $\rho = 0.2$ becomes hollow owing to radiative power loss in the tungsten accumulation phase, as shown in Fig. 5b. This change in the electron temperature profile in the core region can reduce the turbulent outward pinch driven by the TEM [47], which decreases the outward impurity transport. (ii) The increase in electron density and Z_{eff} during the tungsten accumulation phase can reduce the ITG mode growth rate and particle diffusion [48, 49], producing a peak in ion temperature in the central plasma region, as shown in Fig. 5c. (iii) The reason for the increase in the safety factor in the core region [Fig. 5d] may be that plasma cooling and the increase in Z_{eff} in the accumulation phase alternate the plasma electric conductivity and the current redistribution. Overall, T_i/T_e increases as co-NBI is added, indicating that the turbulent transport is reduced and tungsten accumulation is accelerated. However, there have been no reports that the turbulent transport exhibits Z dependence [50] (that the impurity accumulation increases with charge number Z [51]); thus, another mechanism needs to be considered to explain the observation in Fig. 3.
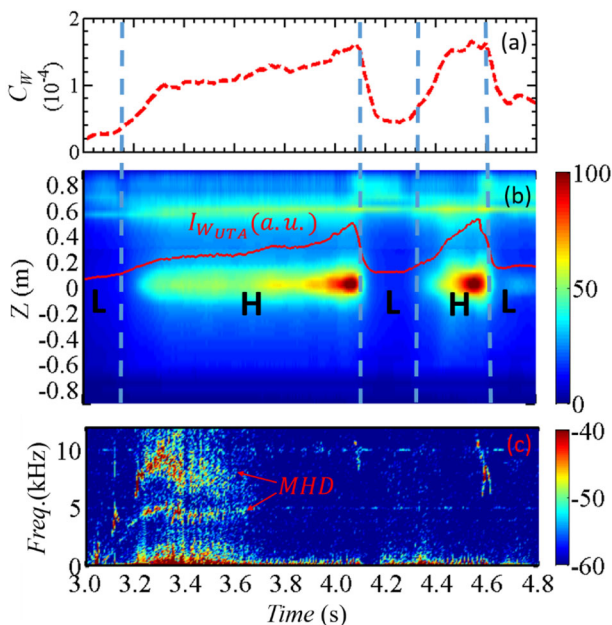
The contribution of neoclassical transport to tungsten accumulation can be indicated by the ratio of the neoclassical radial drift velocity v_{neo} and the diffusion coefficient D_{neo} (v_{neo}/D_{neo}). In this analysis, because the core collisionality is greater than 1, v_{neo}/D_{neo} can be obtained using the simplified expression [10]

$$v_{neo}/D_{neo} = (v_{CL} + v_{PS})/(D_{CL} + D_{PS}), \quad (1)$$

where the subscript CL denotes the classical regime, and PS denotes the Pfirsch–Schlüter regime. According to neoclassical theory, in each regime [10], v/D can be predicted using the expression

$$v = D \frac{Z_I}{Z_D} \left(\frac{1}{n_D} \frac{dn_D}{d\rho} - H \frac{1}{T_D} \frac{dT_D}{d\rho} \right), \quad (2)$$

where n_D and T_D are the main ion density and temperature,

Fig. 5 (Color online) Radial profiles in shot #63723: **a** electron density n_e, **b** electron temperature T_e, **c** ion temperature T_i, and **d** safety factor q. Blue, red, and black lines indicate times in the L-mode phase (3.1 s) and before (3.3 s) and during (4.1 s) the tungsten accumulation phase. ρ is the normalized poloidal flux coordinate, and the dashed black line in **d** indicates $q = 1$
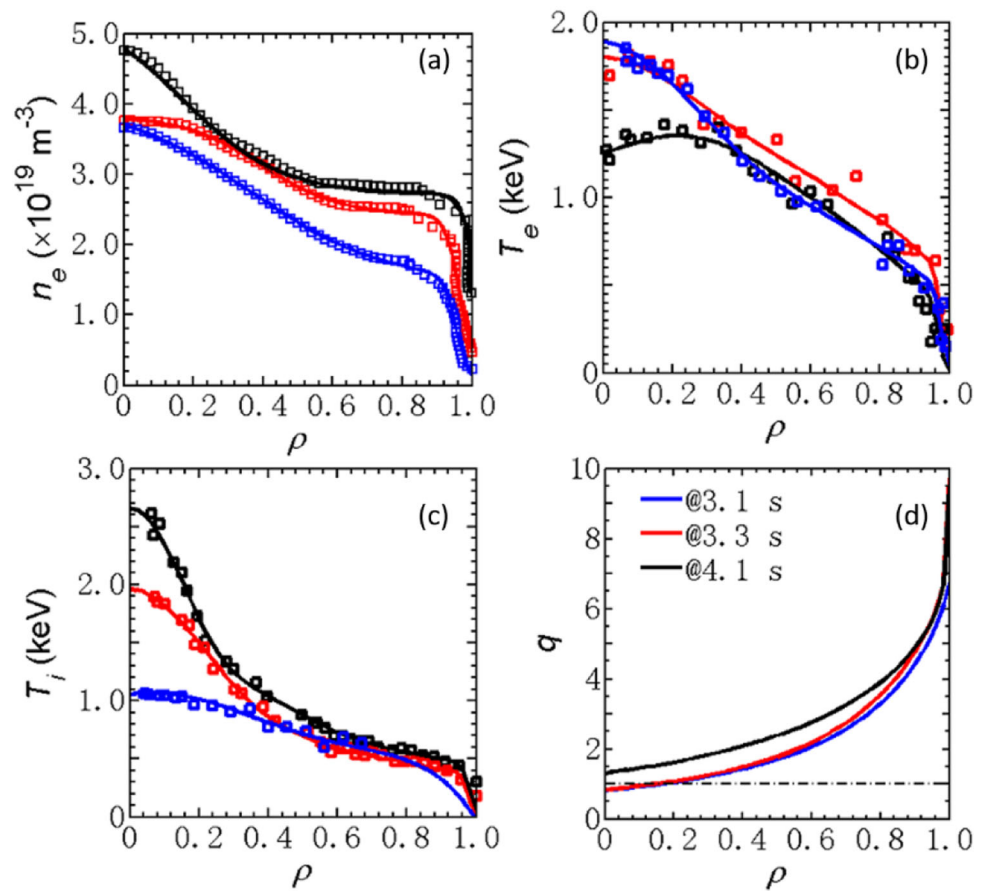
respectively; Z_I is the impurity charge number; and Z_D is the main ion charge number. In the CL regime, $H = 0.5$, and in the PS regime, H is determined by the impurity concentration and collisionality of the main ions. The values of v_{neo}/D_{neo} before and during co-NBI in shot #63723 are estimated assuming $n_D = n_e$ and $T_D = T_i$, and are shown in Fig. 6a. The value of $|v_{neo}/D_{neo}|$ is clearly smaller during the co-NBI phase than before co-NBI, which does not explain the tungsten accumulation observed in this shot.

The PHZ must be taken into account for plasma with a high toroidal rotation velocity [12]. The PHZ velocity is given by the expression

$$v_{PHZ} = \frac{v_{d0}^2}{2Z_0} \frac{C_T C_{\nabla T}}{C_Z^2 + \omega^2}, \qquad (3)$$

where v_{d0} is the magnetic drift velocity, $v_{d0} = mV_t^2/Z_0 eRB$; Z_0 is the impurity ion charge state in ionization equilibrium; ω is the angular frequency of the poloidal motion of impurity ions, $\omega = (V_t - E_r/B_\theta)/(qR_0)$; $C_T = n_e \partial(\gamma_k - \alpha_k)/\partial T_e$;

Fig. 6 (Color online) Estimates of **a** v_{neo}/D_{neo} and **b** $v_{PHZ} + v_{E_r}$ before co-NBI [$V_t(0) \sim 20$ km/s] and during co-NBI [$V_t(0) \sim 140$ km/s] in shot #63723. The shaded areas in **a** are based on the H values, and the dashed lines indicate the averaged v_{neo}/D_{neo}
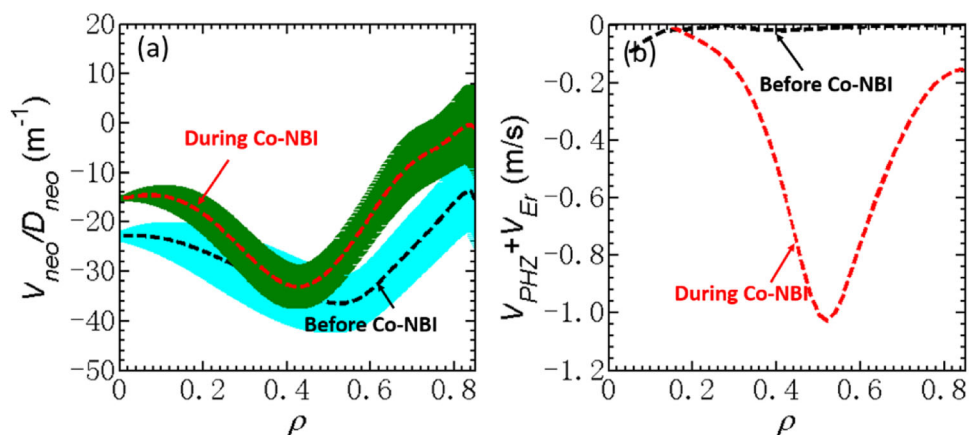
$C_Z = n_e \partial(\gamma_k - \alpha_k)/\partial Z$; and $C_{\nabla T} = dT/d\rho$. In addition, m is the impurity mass, B_θ is the poloidal magnetic field, γ_k is the ionization rate, and α_k is the recombination rate (γ_k and α_k are obtained from [52]). E_r is evaluated using the ion radial force balance equation of the background plasma [53]:

$$E_r = V_t B_\theta - V_p B_t + \frac{\nabla P_i}{Z_i e n_i}, \tag{4}$$

where $P_i = n_i \times T_i$ (n_i is the ion density), and V_p is the poloidal rotation velocity. Because E_r is a function of V_t, the E_r pinch due to the effect of E_r resulting from Coulomb collisions [12] is also considered in this analysis. The E_r pinch is given by the equation.

$$v_{Er} = \Delta r \frac{v_c}{1 + (v_c/\omega)^2}, \tag{5}$$

where Δr is the change in the minor radial position and is expressed as $\Delta r = \frac{(1-2\alpha)k\Delta_0^2}{2(1-\alpha)^3}$ ($\alpha = E_r/V_t B_\theta$, $k = ZeE_r/mV_t^2$, $\Delta_0 = v_{d0}/\omega_0$), and v_c is the collision frequency of impurity ions with the background plasma. The value of v_c for tungsten can be estimated using the expression $v_c \sim Z_W^2(m_D/m_W)^{0.5}v_e^*$, where the electron collisionality is $v_e^* \sim v_{eff}/\varepsilon^{3/2} \sim 10^{-14} n_e Z_{eff} T_e^{-2} R/\varepsilon^{3/2}$ (ε is the inverse aspect ratio). In this work, $v_{PHZ} + v_{E_r}$ is used to evaluate the effect of plasma toroidal rotation velocity on tungsten transport.

To simplify the estimation of $v_{PHZ} + v_{E_r}$ before and during co-NBI, $V_t(0) = 20$ km/s before co-NBI and $V_t(r) = V_t(0)e^{-r/a}$ throughout the plasma radial region are assumed. In the ion radial force balance equation, the second term is not included because V_p is small in the core region, and the third term can be simplified to $\nabla(n_e \times T_i)/en_e$ for bulk plasma. As the toroidal rotation velocity increases from 20 to 140 km/s, the estimated $v_{PHZ} + v_{E_r}$ ($\rho \sim 0.5$) is found to increase from approximately -0.02 m/s to approximately -1.0 m/s, as shown in Fig. 6b, which results in increased inward transport of tungsten and causes tungsten accumulation. Because the PHZ velocity depends strongly on the impurity mass, the increase in inward pinch velocity v_{PHZ} (from approximately -0.017 m/s to approximately -0.8 m/s around $\rho = 0.5$) can explain why tungsten accumulates more easily than other impurities (Fig. 3).

3.2 Tungsten control using counter-NBI and favorable B_t

To suppress or avoid tungsten accumulation in NBI-heated ELMy H-mode plasmas, the values of T_i/T_e, v_{neo}/D_{neo}, and $v_{PHZ} + v_{E_r}$ should be decreased. For this purpose, counter-NBI is applied to modify the density and

temperature and brake the plasma toroidal rotation. Normally, the counter-NBI is not good for plasma confinement other than the co-NBI because counter-NBI introduces impurities into the main plasma and degrades the confinement [54]. To rule out the possibility that the decreased tungsten content is due to the loss of confinement, another mechanism is needed for reducing the penetration of impurities into the main plasma and compensating for plasma confinement. It has been found that a favorable B_t (in the co-I_p direction, where the direction of $B_t \times \nabla B_t$ points toward the X-point) can improve plasma confinement [55] (compared with an unfavorable B_t, a favorable B_t can improve the H_{98} by $\sim 20\%$ in shots with similar plasma parameters). In addition, favorable B_t is found to have a positive effect on tungsten control, which will be discussed in the next section. For these reasons, the tungsten behavior was investigated using counter-NBI with a favorable B_t direction, as in shot #71605. As shown in Fig. 7, type-I ELMs with $f_{ELM} \sim 40$ Hz were obtained when additional co-NBI was performed during the LHW heating phase. This shot was the last shot before lithium wall conditioning and was performed in the USN
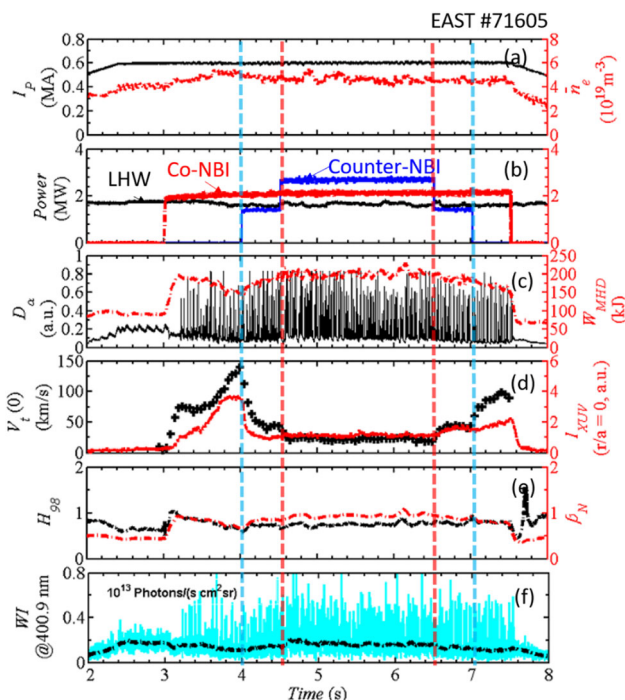
Fig. 7 (Color online) Waveforms of EAST shot #71605: **a** plasma current I_p and line-averaged electron density $\bar{n}_e$, **b** source power of LHW and NBI (co- and counter-injection directions), **c** D_α emission signal from upper divertor and plasma stored energy W_{MHD}, **d** central toroidal rotation velocity $V_t(0)$ and XUV emission signals at $r/a = 0$, **e** energy confinement factor H_{98} and normalized beta β_N, **f** tungsten influx at inner target plate, where the black line denotes its tendency. The tungsten flux is indicated by the intensity of the WI emission line at 400.9 nm from the filterscope diagnostic [42]

configuration with $B_t = 2.4$ T, $I_p = 0.6$ MA, $\bar{n}_e \sim 4.2 \times 10^{19}$ m^{-3}, $q_{95} = 4.8$, and maximum source powers of LHW and NBI of 1.6 and 4.8 MW, respectively.

The central radiation (as indicated by the central XUV emission intensity) clearly decreases rapidly when counter-NBI is performed, although counter-NBI slightly enhances the tungsten source (as indicated by the intensity of W I line emission at 400.9 nm) near the upper divertor region. Further analysis shows that the evolution of C_W is directly correlated with the control of $V_t(0)$ by co- and counter-NBI. As shown in Fig. 7d, when co-NBI heating with a 2 MW source power is applied at 3.0 s, $V_t(0)$ begins to increase and reaches a peak value of approximately 150 km/s. As shown in Fig. 8a and b, the increase in plasma toroidal rotation velocity results in a rapid increase in C_W and a gradual peak in the W-UTA emission intensity measured by EUV_Long2. EUV_Long2 [56] is a newly developed space-resolved EUV spectrometer that can provide the radial profile of impurity line emission covering a wide vertical range of -0.085 m $\leq Z \leq 0.4$ m [Fig. 12b]. These rapid variations in C_W and the W-UTA profile in the core region suggest tungsten accumulation. However, C_W decreases and the W-UTA emission intensity in the core plasma suddenly dissipates when counter-NBI heating with a 1.4 MW source power is superimposed at 4.0 s to reduce $V_t(0)$ to 45 km/s. When the counter-NBI source power is increased to 2.8 MW, $V_t(0)$ can be further reduced and finally maintained at ~ 20 km/s. When the counter-NBI source power decreases and vanishes, C_W increases again with the increase in $V_t(0)$. In addition, additional peaks in the W-UTA emission intensity in the core region indicate that tungsten accumulation again occurs. In this process,
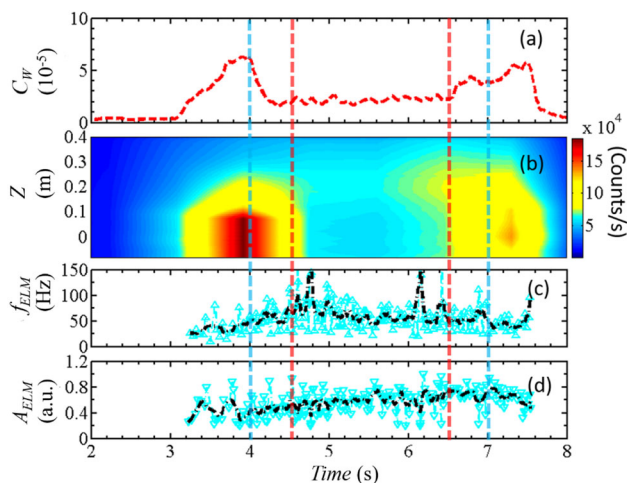

Fig. 8 (Color online) Time evolution of **a** tungsten concentration C_W, **b** contour plot of W-UTA emission intensity measured by a newly developed space-resolved EUV spectrometer (EUV_Long2 in Fig. 1), **c** frequency of ELMs f_{ELM}, and **d** normalized amplitude of ELMs A_{ELM} (black lines indicate their tendency) in shot #71605

when counter-NBI with a maximum power of 2.8 MW is added during the co-NBI phase, $V_t(0)$ changes from 150 to 20 km/s. Consequently, C_W decreases from $\sim 7 \times 10^{-5}$ to $\sim 2 \times 10^{-5}$; thus, the power radiation fraction P_{rad}/P_{total} is decreased from $\sim 32\%$ to $\sim 8\%$.

In the ELMy H-mode phase, the superimposed counter-NBI also changes the characteristics of ELMs [57] (such as frequency f_{ELM} and amplitude A_{ELM}), as shown in Fig. 8 (c) and (d). It has been found that high-frequency ELMs can provide continuous transport of impurities in the edge plasma region, which prevents the accumulation of impurities [58–60]. This effect of ELMs on the elimination of impurities is called impurity flushing. The correlation analysis of $V_t(0)$, f_{ELM}, and C_W from 4 to 4.55 s shows that C_W is strongly dependent on $V_t(0)$ but weakly dependent on f_{ELM}. This weak dependence of C_W on f_{ELM} results from the fact that the low-frequency ELMs (which increase from ~ 50 to ~ 65 Hz during that time period) are insufficiently effective in flushing out impurities [58]. Note also that no core MHD activity is observed on the spectrogram of the central chord of the soft X-ray emission signals, and the energy confinement factor H_{98} remains nearly constant during the counter-NBI heating phase. This result implies that the counter-NBI added here does not degrade the plasma confinement and can effectively suppress tungsten accumulation in the type-I ELMy H-mode on EAST.

However, the decrease in C_W during the added counter-NBI phase is attributed not only to the reduced toroidal rotation velocity, but also to the variations in density and temperature and their gradients. Figure 9a–c shows the density and temperature profiles at time points before (at 3.5 s, red line), during (at ~ 5.0 s, blue line), and after (at ~ 7.0 s, black line) counter-NBI in shot #71605. Under the assumption described above, the estimated $v_{PHZ} + v_{Er}$ ($\rho \sim 0.4$) decreases from approximately -0.57 m/s to approximately -0.02 m/s when the counter-NBI changes $V_t(0)$ from ~ 80 to ~ 20 km/s, as shown in Fig. 10 (b). The figure also shows that the applied counter-NBI increases the density and flattens its profile in the region $0.3 < \rho < 0.9$ and clearly enhances the ion temperature and its gradient inside $\rho \sim 0.7$. These changes will increase the impurity diffusivity owing to the enhanced collisionality [61] and may decrease the pinch velocity of impurities in the central region.

The values of v_{neo}/D_{neo} in the co-NBI and counter-NBI phases in shot #71605 were also estimated and are shown in Fig. 10a. When counter-NBI is added during the co-NBI phase, v_{neo}/D_{neo} outside of $\rho \sim 0.2$ can be reduced, and the direction of v_{neo}/D_{neo} can even be reversed from inward to outward around $\rho = 0.6$. The reversed direction is determined by the ratio of the normalized temperature gradient to the normalized main ion density gradient,
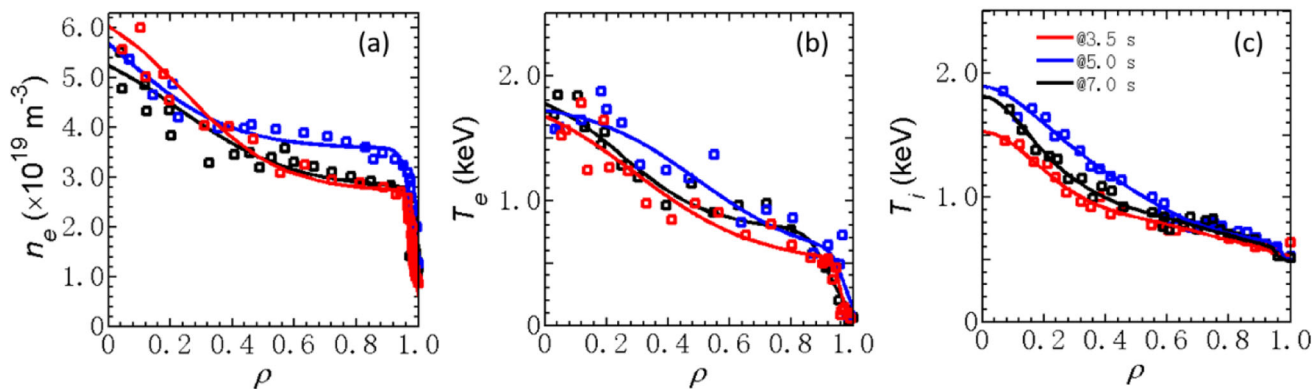
Fig. 9 (Color online) Radial profiles of shot #71605: **a** electron density n_e, **b** electron temperature T_e, and **c** ion temperature T_i. Red, blue, and black lines indicate times before (3.5 s), during (5.0 s), and after (7.0 s) counter-NBI, respectively

Fig. 10 (Color online) Estimated **a** v_{neo}/D_{neo} and **b** $v_{PHZ} + v_{Er}$ during co-NBI [$V_t(0) \sim 80$ km/s] and added counter-NBI [$V_t(0) \sim 20$ km/s] in shot #71605. The shaded areas in **a** are based on the H values, and the dashed lines indicate the average v_{neo}/D_{neo}
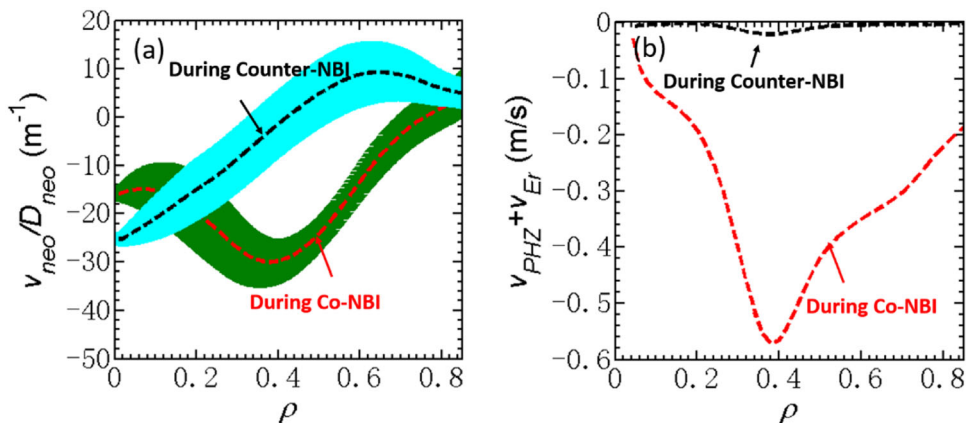

$\eta_D = \frac{1}{T_D} \frac{dT_D}{dr} / \frac{1}{n_D} \frac{dn_D}{dr}$. It is inferred that the added counter-NBI in this shot reduces the PHZ + E_r inward pinch velocity and weakens the contribution of neoclassical inward transport. Note, however, that T_i/T_e increases slightly when counter-NBI is added, which should reduce the turbulent impurity transport and increase tungsten accumulation. Thus, it can be concluded that the decrease in C_W during the counter-NBI phase is not caused by turbulent transport.

3.3 Effect of favorable B_t on tungsten control

In this section, the effect of B_t direction on tungsten control is discussed. It was found that the impurity confinement time (τ_{imp}) was significantly reduced in favorable B_t experiments in recent EAST campaigns. Typically, τ_{imp} can be reduced by nearly half for favorable B_t H-mode plasmas (e.g., $\tau_{imp} \sim 112.0$ ms for unfavorable B_t in shot #79062 and $\tau_{imp} \sim 61.2$ ms for favorable B_t in shot #80303). Shots #79062 and #80303 are similar shots that have opposite B_t directions [55]. The effect was further studied by investigating C_W and the tungsten flux in the divertor. To decrease the effect of toroidal rotation velocity

on tungsten transport, the shots with low $V_t(0)$ (< 30 km/s) are chosen for comparison. C_W versus $V_t(0)$ in steady-state ELMy H-mode discharges with unfavorable and favorable B_t directions is compared in Fig. 11. The selected shots have the following parameters: $I_p = 0.45$–0.55 MA, $\bar{n}_e = 2.8$–4.5×10^{19} m^{-3}, and the total heating powers are similar. This figure shows that C_W can be easily controlled below 8×10^5 in the ELMy H-mode plasmas with reduced toroidal rotation velocity [$V_t(0) < 30$ km/s], where C_W is generally lower in the shots with favorable B_t direction than in those with unfavorable B_t direction. These two B_t directions produce $E_r \times B$ drift with opposite poloidal directions, as shown in Fig. 11c. For the unfavorable B_t direction, the divertor $E_r \times B$ drift increases the backflow (PS flow) of impurity particles from the upper outer divertor to the upstream region. For the favorable B_t direction, the backflow of impurity particles is directed to the lower divertor and can be exhausted by the closed divertor structure [62]. The lower divertor structure is closed because it is W-shaped with a dome. This effect partially explains the lower C_W in the shots with the favorable B_t direction. In addition, the $E_r \times B$ drift in the favorable B_t direction increases the tungsten flux on the
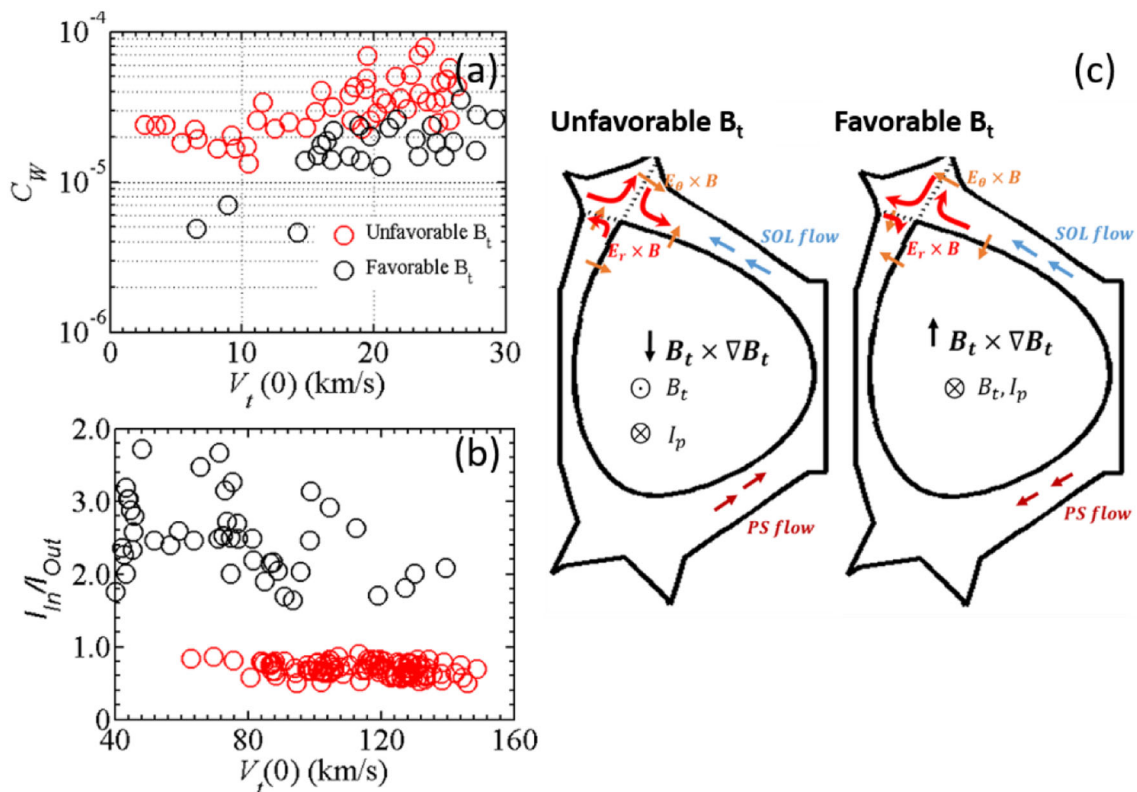
Fig. 11 (Color online) **a** Tungsten concentration versus toroidal rotation velocity in ELMy H-mode plasmas with parameters of $I_p = 0.45$–0.6 MA and $\bar{n}_e = 2.8$–4.5 $\times$ 10^{19} m^{-3}, **b** ratio of tungsten flux density near the inboard and outboard sides (I_{In}/I_{Out}) in shots with unfavorable (red) and favorable B_t (black) directions, and **c** schematic diagram of drifts and parallel flows in the corresponding USN configuration

inboard side [as indicated by the increased I_{In}/I_{Out} shown in Fig. 11b], which may affect tungsten transport in the core region owing to the poloidal asymmetry of the tungsten density when the toroidal rotation velocity is low. The in–out asymmetry effect is beneficial for removing the tungsten from the core plasma [63–65], for example, by reversing the direction of v_{neo}/D_{neo} from inward to outward.

The W-UTA emission intensity profiles in ELMy H-mode plasmas with different $B_t \times \nabla B_t$ drift directions are presented in Fig. 12a. To eliminate the effect of electron temperature on tungsten transport, two shots with similar magnetic axes (near $Z = 0.024$ m) and central electron temperatures are compared. Figure 12a shows that the W-UTA emission intensity profile is flatter for the favorable B_t direction than for the unfavorable B_t direction. The flatter W-UTA emission intensity profile suggests that the favorable B_t direction is beneficial for avoiding tungsten accumulation and can decrease the risk of intense radiated power in the core region. From these facts, it can be deduced that lower C_W with favorable B_t will expand the operating window toward steady-state type-I ELMy H-mode operation.

4 Summary and discussion

The tungsten behavior in ELMy H-mode plasmas with co-/counter-NBI and unfavorable/favorable B_t on EAST was investigated. The results showed that tungsten always accumulates in ELMy H-mode plasma with co-NBI owing to the increased inward pinch velocity $v_{PHZ} + v_{E_r}$ and decreased turbulent transport. C_W can exceed 10^{-4} in the type-I ELMy H-mode with $V_t(0) > 120$ km/s and unfavorable B_t, ultimately resulting in the degradation of plasma confinement and periodic H–L transitions. Thus, C_W must be maintained below 10^{-4} for future steady-state type-I ELMy H-mode operation on EAST.

To suppress and avoid tungsten accumulation in ELMy H-mode plasmas, both the neoclassical inward convection and PHZ inward pinch velocities should be decreased, whereas turbulent transport needs to be increased. For this purpose, counter-NBI was applied to modify the density and temperature and brake the plasma toroidal rotation. The result shows that C_W can be decreased from $\sim 7 \times 10^{-5}$ to $\sim 2 \times 10^{-5}$ in the type-I ELMy H-mode plasma with favorable B_t when counter-NBI is superimposed during the co-NBI heating phase. The

Fig. 12 (Color online)
a Comparison of W-UTA
emission intensity profiles in
type-I ELMy H-mode plasmas
with unfavorable and favorable
B_t directions, **b** viewing range of
space-resolved EUV
spectrometer (blue) and plasma
shape in the shots with
unfavorable (red) and favorable
(black) B_t directions in EAST
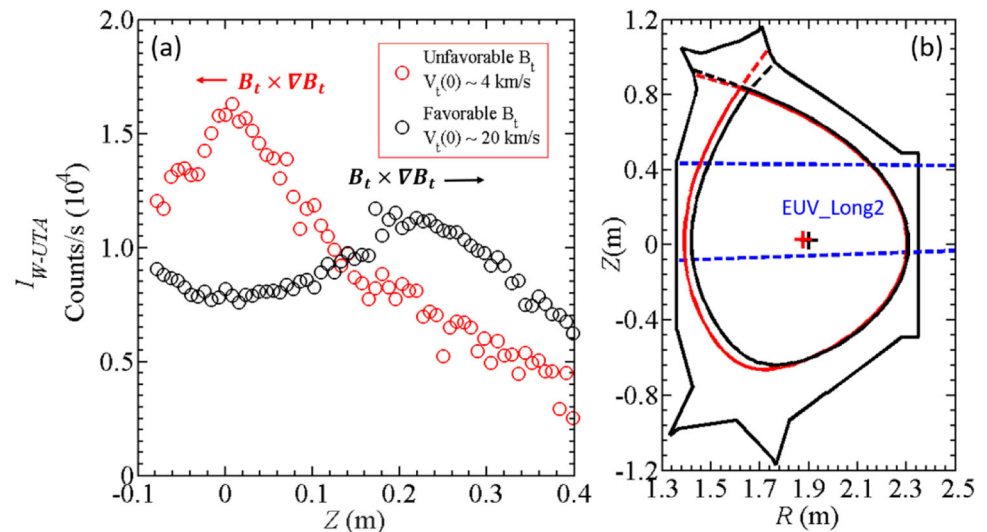
analysis indicated that the added counter-NBI not only decreases the PHZ + E_r inward pinch velocity but also reverses the v_{neo}/D_{neo} direction from inward to outward; both of these changes contribute to the suppression of tungsten accumulation. It was preliminarily found that, because NBI directly heats ions, turbulent transport in the core region driven by co-/counter-NBI is disadvantageous for the suppression of tungsten accumulation. Increasing the turbulent transport during the co-/counter-NBI phases by increasing the power of LHW heating or adopting on-axis electron cyclotron resonance heating is required. Further detailed studies remain as future work.

It was also found that C_W is lower in ELMy H-mode plasmas with favorable B_t than in similar discharges with unfavorable B_t. Possible reasons for the effect of B_t direction on C_W were discussed. On the one hand, in discharges with favorable B_t in the USN configuration, the backflow of impurity particles is directed to the lower divertor and can be exhausted by the closed divertor structure. On the other hand, in low-rotation plasmas, the $E_r \times B$ drift in plasmas with favorable B_t increases the tungsten flux on the inboard side, which can weaken the contribution of neoclassical inward convection because of in–out asymmetry.

These results demonstrate the potential of counter-NBI in the favorable B_t direction for suppressing tungsten accumulation in ELMy H-mode plasma. The application of counter-NBI to suppress tungsten accumulation and avoid plasma confinement degradation must ensure that V_t and I_p have the same direction ($V_t > 0$), that V_t is sufficiently low, and that B_t is favorable. Otherwise, impurities can accumulate more easily during counter-NBI than during co-NBI [12, 54], which destroys the plasma confinement. The lower C_W in the core plasma caused by counter-NBI in the favorable B_t direction will extend the operating window for

exploring steady-state type-I ELMy H-mode operation in EAST in the near future.

References

1. R.C. Isler, Impurities in tokamak. Nucl. Fusion **24**, 1599–1678 (1984). https://doi.org/10.1088/0029-5515/24/12/008
2. E.Z. Li, L. Xu, W. Guo et al., Understanding the destabilization of a resistive drift mode in EAST core plasmas. Phys. Plasma **24**, 022504 (2017). https://doi.org/10.1063/1.4976136
3. J.A. Wesson, R.D. Gill, M. Hugon et al., Disruptions in JET. Nucl. Fusion **29**, 641 (1989). https://doi.org/10.1088/0029-5515/29/4/009
4. R.C. Isler, W.L. Roman, W.L. Hodge, Long-time impurity confinement as a precursor to disruption in ohmically heated tokamaks. Phys. Rev. Lett. **55**, 2413 (1985). https://doi.org/10.1103/physrevlett.55.2413
5. D.H. Zhu, C.J. Li, R. Li et al., Characterization of the in situ leading-edge-induced melting on the ITER-like tungsten divertor in EAST. Nucl. Fusion **60**, 016036 (2020). https://doi.org/10.1088/1741-4326/ab561e
6. T. Püetterich, R. Dux, R. Neu et al., Observations on the W-transport in the core plasma of JET and ASDEX upgrade. Plasma Phys. Control. Fusion **55**, 124036 (2013). https://doi.org/10.1088/0741-3335/55/12/124036
7. M. Mayer, M. Andrzejczuk, R. Dux et al., Tungsten erosion and redeposition in the all-tungsten divertor of ASDEX upgrade. Phys. Scr. **2009**, 014039 (2009). https://doi.org/10.1088/0031-8949/2009/t138/014039

8. T. Pütterich, R. Dux, M.N.A. Beurskens *et al.,* Tungsten screening and impurity control in JET, in Paper Presented at *24th IAEA Conference on Fusion Energy, San Diego, USA* 8–13 Oct. (2012). https://juser.fz-juelich.de/record/134562

9. S.Y. Shi, X. Jian, V.S. Chan et al., Evaluating the effects of tungsten on CFTER phase I performance. Nucl. Fusion **58**, 126020 (2018). https://doi.org/10.1088/1741-4326/aae397

10. S.P. Hirshman, D.J. Sigmar, Neoclassical transport of impurities in tokamak plasmas. Nucl. Fusion **21**, 1079–1201 (1981). https://doi.org/10.1088/0029-5515/21/9/003

11. H. Maassberg, R. Brakel, R. Burhenn et al., Transport in stellarators. Plasma Phys. Control. Fusion **35**, B319–B332 (1993). https://doi.org/10.1088/0741-3335/35/sb/026

12. K. Hoshino, M. Toma, K. Shimizu et al., Inward pinch of high-Z impurity in a rotating tokamak plasma: effects of atomic processes, radial electric field and Coulomb collisions. Nucl. Fusion **51**, 083027 (2011). https://doi.org/10.1088/0029-5515/51/8/083027

13. R.C. Isler, L.E. Murray, E.C. Crume et al., Impurity transport and plasma rotation in the ISX-B tokamak. Nucl. Fusion **23**, 1017 (1983). https://doi.org/10.1088/0029-5515/23/8/003

14. T. Nakano and The JT-60 Team, Tungsten transport and accumulation in JT-60U. J. Nucl. Mater. **415**, S327–S333 (2011). https://doi.org/10.1016/j.jnucmat.2010.12.020

15. R. Neu, R. Dux, A. Geier et al., Impurity behaviour in the ASDEX upgrade divertor tokamak with large area tungsten walls. Plasma Phys. Control. Fusion **44**, 811 (2002). https://doi.org/10.1088/0741-3335/44/6/313

16. P. Helander, D.J. Sigmar, *Collisional Transport in Magnetized Plasmas* (Cambridge University Press, Cambridge, 2002)

17. Y. Nakamura, N. Tamura, M. Yoshinuma et al., Strong suppression of impurity accumulation in steady-state hydrogen discharges with high power NBI heating on LHD. Nucl. Fusion **57**, 056003 (2017). https://doi.org/10.1088/1741-4326/aa6187

18. H. Nordman, A. Skyman, P. Strand et al., Fluid and gyrokinetic simulations of impurity transport at JET. Plasma Phys. Control. Fusion **53**, 105005 (2011). https://doi.org/10.1088/0741-3335/53/10/105005

19. C. Estrada-Mila, J. Candy, R.E. Waltz, Gyrokinetic simulations of ion and impurity transport. Phys. Plasma **12**, 022305 (2005). https://doi.org/10.1063/1.1848544

20. T. Fülöp, H. Nordman, Turbulent and neoclassical impurity transport in tokamak plasmas. Phys. Plasma **16**, 032306 (2009). https://doi.org/10.1063/1.3083299

21. C. Angioni, F.J. Casson, P. Mantica et al., The impact of poloidal asymmetries on tungsten transport in the core of JET H-mode plasmas. Phys. Plasmas **22**, 055902 (2015). https://doi.org/10.1063/1.4919036

22. C. Angioni, P. Mantica, T. Püetterich et al., Tungsten transport in JET H-mode plasmas in hybrid scenario, experimental observations and modelling. Nucl. Fusion **54**, 083028 (2014). https://doi.org/10.1088/0029-5515/54/8/083028

23. T. Odstrcil, T. Püetterich, C. Angioni et al., The physics of W transport illuminated by recent progress in W density diagnostics at ASDEX Upgrade. Plasma Phys. Control. Fusion **60**, 014003 (2018). https://doi.org/10.1088/1361-6587/aa8690

24. T. Wegnerl, J.A. Alcusónl, B. Geiger et al., Impact of the temperature ratio on turbulent impurity transport in Wendelstein 7-X. Nucl. Fusion **60**, 124004 (2020). https://doi.org/10.1088/1741-4326/abb869

25. C. Angioni, Gyrokinetic study of the impact of the electron to ion heating ratio on the turbulent diffusion of highly charged impurities. Phys. Plasmas **22**, 102501 (2015). https://doi.org/10.1063/1.4932070

26. L. Zhang, S. Morita, Z. Xu et al., Suppression of tungsten accumulation during ELMy H-mode by lower hybrid wave heating in the EAST tokamak. Nucl. Mater. Energy **12**, 774–778 (2017). https://doi.org/10.1016/j.nme.2017.01.009

27. Q.Q. Yang, G.S. Xu, N. Yan et al., Stationary high-performance grassy ELM regime in EAST. Nucl. Fusion **60**, 076012 (2020). https://doi.org/10.1088/1741-4326/ab8e0f

28. Y.C. Shen, H.M. Zhang, B. Lyu et al., Measurement of molybdenum ion density for L-mode and H-mode plasma discharges in the EAST tokamak. Chin. Phys. B **29**, 065206 (2020). https://doi.org/10.1088/1674-1056/ab8456

29. X.J. Zhang, Y.P. Zhao, X.Z. Gong et al., Steady state plasma operation in RF dominated regimes on EAST. AIP Conf. Proc. **1689**, 030012 (2015). https://doi.org/10.1063/1.4936477

30. Z. Chen, Y.P. Zhao, G. Chen et al., Design and implementation of power and phase feedback control system for ICRH on EAST. Nucl. Sci. Tech. **29**(2), 19 (2018). https://doi.org/10.1007/s41365-018-0362-8

31. Z.X. Cui, X. Li, S.B. Shu et al., Calculation of the heat flux in the lower divertor target plate using an infrared camera diagnostic system on the experimental advanced superconducting Tokamak. Nucl. Sci. Tech. **30**(6), 94 (2019). https://doi.org/10.1007/s41365-019-0625-z

32. D.M. Yao, G.N. Luo, S.J. Du et al., Overview of the EAST in-vessel components upgrade. Fusion Eng. Des. **98**, 1692–1695 (2015). https://doi.org/10.1016/j.fusengdes.2015.06.084

33. C.D. Hu for the NBI team, First achievement of plasma heating for EAST neutral beam injector. Plasma Sci. Technol. **17**, 1–3 (2015). https://doi.org/10.1088/1009-0630/17/1/01

34. L. Tao, C.D. Hu, Y.L. Xie, Thermodynamic analysis and simulation for gas baffle entrance collimator of EAST-NBI system based on thermo-fluid coupled method. Nucl. Sci. Tech. **29**(1), 2 (2018). https://doi.org/10.1007/s41365-017-0349-x

35. L. Li, L. Zhang, Z. Xu et al., Line identification of extreme ultraviolet (EUV) spectra from low-Z impurity ions in EAST tokamak plasmas. Plasma Sci. Technol. **23**, 075102 (2021). https://doi.org/10.1088/2058-6272/abfea2

36. L. Zhang, S. Morita, Z. Xu et al., A fast-time-response extreme ultraviolet spectrometer for measurement of impurity line emissions in the experimental advanced superconducting Tokamak. Rev. Sci. Instrum. **86**, 123509 (2015). https://doi.org/10.1063/1.4937723

37. S.B. Shu, C.M. Yu, C. Chao et al., Improved plasma position detection method in EAST Tokamak using fast CCD camera. Nucl. Sci. Tech. **30**(2), 24 (2019). https://doi.org/10.1007/s41365-019-0549-7

38. X. Gao, Y. Yang, T. Zhang et al., Key issues for long-pulse high-β_N operation with the experimental advanced superconducting Tokamak (EAST). Nucl. Fusion **57**, 056021 (2017). https://doi.org/10.1088/1741-4326/aa626c

39. B.N. Wan, Y.F. Liang, X.Z. Gong et al., Overview of EAST experiments on the development of high-performance steady-state scenario. Nucl. Fusion **57**, 102019 (2017). https://doi.org/10.1088/1741-4326/aa7861

40. B.N. Wan, J.G. Li, H.Y. Guo et al., Advances in H-mode physics for long-pulse operation on EAST. Nucl. Fusion **55**, 104015 (2015). https://doi.org/10.1088/0029-5515/55/10/104015

41. B.N. Wan and EAST team, A new path to improve high β_P plasma performance on EAST for steady-state Tokamak fusion reactor. Chin. Phys. Lett. **37**, 045202 (2020). https://doi.org/10.1088/0256-307X/37/4/045202

42. Z. Xu, Z.W. Wu, W. Gao et al., Filterscope diagnostic system on the experimental advanced superconducting Tokamak (EAST). Rev. Sci. Instrum. **87**, 11D429 (2016). https://doi.org/10.1063/1.4961294

43. J. Ou, N. Xiang, Z.Z. Men et al., Estimation of tungsten production from the upper divertor in EAST during edge localized

modes. Chin. Phys. B **28**, 125201 (2019). https://doi.org/10.1088/1674-1056/ab5279

44. X.D. Yang *et al., Plasma Phys. Control. Fusion* submitted (2020)

45. T.C. Hender, P. Buratti, F.J. Casson et al., The role of MHD in causing impurity peaking in JET hybrid plasmas. Nucl. Fusion **56**, 066002 (2016). https://doi.org/10.1088/0029-5515/56/6/066002

46. M. Sertoli, R. Dux, T. Pütterich et al., Modification of impurity transport in the presence of saturated ($m,$ n) = (1,1) MHD activity at ASDEX upgrade. Plasma Phys. Control. Fusion **57**, 075004 (2015). https://doi.org/10.1088/0741-3335/57/7/075004

47. A. Mollén, I. Pusztai, T. Fülöp et al., Impurity transport in trapped electron mode driven turbulence. Phys. Plasma **20**, 032310 (2013). https://doi.org/10.1063/1.4796196

48. J. Li, Z.X. Wang, J.Q. Dong et al., Impurity effects on ion temperature gradient driven multiple modes in transport barriers. Nucl. Fusion **59**, 076013 (2019). https://doi.org/10.1088/1741-4326/ab0ee2

49. G.R. McKee, M. Murakami, J.A. Boedo et al., Impurity-induced turbulence suppression and reduced transport in the DIII-D tokamak. Phys. Plasmas **7**, 1870 (2000). https://doi.org/10.1063/1.874010

50. T. Parisot, R. Guirlet, C. Bourdelle et al., Experimental impurity transport and theoretical interpretation in a Tore Supra lower-hybrid heated plasma. Plasma Phys. Control. Fusion **50**, 055010 (2008). https://doi.org/10.1088/0741-3335/50/5/055010

51. K. Ida, R.J. Fonck, C. Sesnic et al., Observation of Z-dependent Impurity accumulation in the PBX Tokamak. Phys. Rev. Lett. **58**, 116–119 (1987). https://doi.org/10.1103/PhysRevLett.58.116

52. OPEN-ADAS home page. http://open.adas.ac.uk/

53. J.W. Coenen, O. Schmitz, B. Unterberg et al., Rotation and radial electric field in the plasma edge with resonant magnetic perturbation at TEXTOR. Nucl. Fusion **51**, 063030 (2011). https://doi.org/10.1088/0029-5515/51/6/063030

54. R.C. Isler, P.D. Morgan, N.J. Peacock, Impurity accumulation in ISX-B during counter-injection—are alternative hypotheses valid? Nucl. Fusion **25**, 386–392 (1985). https://doi.org/10.1088/0029-5515/25/3/013

55. X. Lin, Q.Q. Yang, G.S. Xu et al., Plasma performance improvement with favourable B_t relative to unfavourable B_t in RF-heated H-mode plasmas in EAST. Nucl. Fusion **61**, 026014 (2021). https://doi.org/10.1088/1741-4326/abcb27

56. L. Zhang, S. Morita, Z.W. Wu et al., A space-resolved extreme ultraviolet spectrometer for radial profile measurement of tungsten ions in the experimental advanced superconducting Tokamak. Nucl. Inst. Methods Phys. Res. A **916**, 169–178 (2019). https://doi.org/10.1016/j.nima.2018.11.082

57. N. Oyama, Y. Kamada, A. Isayama et al., ELM frequency dependence on toroidal rotation in the grassy ELM regime in JT-60U. Plasma Phys. Control. Fusion **49**, 249–259 (2007). https://doi.org/10.1088/0741-3335/49/3/005

58. D.C. van Vugt, G.T.A. Huijmans, M. Hoelzl et al., Kinetic modeling of ELM-induced tungsten transport in a tokamak plasma. Phys. Plasmas **26**, 042508 (2019). https://doi.org/10.1063/1.5092319

59. T. Püetterich, R. Dux, M.A. McDermott et al., ELM flushing and impurity transport in the H-mode edge barrier in ASDEX Upgrade. J. Nucl. Mater. **415**, S334–S339 (2011). https://doi.org/10.1016/j.jnucmat.2010.09.052

60. M.R. Wade, K.H. Burrell, A.W. Leonard et al., Edge-localized-mode-induced transport of impurity density, energy, and momentum. Phys. Rev. Lett. **94**, 225001 (2005). https://doi.org/10.1103//PhysRevLett.94.225001

61. R. Dux, A.G. Peeters, A. Gude et al., Z dependence of the core impurity transport in ASDEX Upgrade H mode discharges. Nucl. Fusion **39**, 1509 (1999). https://doi.org/10.1088/0029-5515/39/11/302

62. Y.W. Yu, L. Wang, B. Cao et al., Fuel retention and recycling studies by using particle balance in EAST tokamak. Phys. Scr. **T170**, 014070 (2017). https://doi.org/10.1088/1402-4896/aa8fd9

63. A. Mollén, I. Pusztai, T. Fülöp et al., Effect of poloidal asymmetries on impurity peaking in tokamaks. Phys. Plasma **19**, 052307 (2012). https://doi.org/10.1063/1.4719711

64. C. Angioni, P. Helander, Neoclassical transport of heavy impurities with poloidally asymmetric density distribution in tokamaks. Plasma Phys. Control. Fusion **56**, 124001 (2014). https://doi.org/10.1088/0741-3335/56/12/124001

65. S. Espinosa, P.J. Catto, Pedestal radial flux measuring method to prevent impurity accumulation. Phys. Plasmas **24**, 055904 (2017). https://doi.org/10.1063/1.4978886